Quantum Oscillator Noise Spectroscopy via Displaced Cat States

Alistair R. Milne,[1,*] Cornelius Hempel,[1,‡] Li Li,[2] Claire L. Edmunds,[1] Harry J. Slatyer,[2] Harrison Ball,[2] Michael R. Hush,[2] and Michael J. Biercuk[1,2,†]

[1]ARC Centre of Excellence for Engineered Quantum Systems, The University of Sydney, School of Physics, New South Wales 2006, Australia

[2]Q-CTRL Pty Ltd, Sydney, New South Wales 2006, Australia

(Received 20 October 2020; accepted 21 April 2021; published 25 June 2021)

Quantum harmonic oscillators are central to many modern quantum technologies. We introduce a method to determine the frequency noise spectrum of oscillator modes through coupling them to a qubit with continuously driven qubit-state-dependent displacements. We reconstruct the noise spectrum using a series of different drive phase and amplitude modulation patterns in conjunction with a data-fusion routine based on convex optimization. We apply the technique to the identification of intrinsic noise in the motional frequency of a single trapped ion with sensitivity to fluctuations at the sub-Hz level in a spectral range from quasi-dc up to 50 kHz.

DOI: 10.1103/PhysRevLett.126.250506

Harmonic oscillators and their quantized excitations play a crucial role in many quantum systems relevant to quantum information processing. In trapped-ion [1–4], many superconducting [5–8], and also electron spin-based [9] architectures, they mediate qubit-qubit interactions in the form of motional modes carrying phonons or microwave resonators storing photons, respectively. Optomechanical coupling between the quantum motion of microresonators and photons may also be used as a universal transducer between stationary and optical qubits [10]. Furthermore, in both trapped-ion and superconducting platforms, the oscillators themselves have been used to realize a logical qubit encoded in coherent superposition states [11,12], allowing for an efficient implementation of a bosonic quantum error correcting code [13]. In these systems, oscillator frequency fluctuations are often a limiting error source, degrading the mediated interactions and encoded bosonic states. Such fluctuations have been probed in trapped ions using coherent displacements [14,15] and large superpositions of number states [15,16]. Noise spectroscopy of the oscillator system can identify performance-limiting error sources, assess their relative weights, and inform appropriately tailored error-mitigation strategies through quantum control engineering [17].

In this Letter, we experimentally demonstrate a method for the spectrally resolved sensing of harmonic oscillator frequency fluctuations that is based on the interference of cat states [18]. The deterministic generation of oscillator cat states has been demonstrated in a variety of systems [19–23], and interference of the oscillator wave packets has previously been applied to single photon detection [24]. Here, we apply a continuously driven qubit-state-dependent displacement to the motional wave packet of a single trapped ion, while inverting the drive phase at regular intervals to tune the protocol's peak sensitivity in frequency space. We combine this phase modulation with a shaped amplitude envelope defined by bandlimited Slepian functions [25–27] to suppress spurious signatures arising from spectral leakage at harmonics of the peak sensitivity. The modulation pattern and pulse shape of the driving field translate to a filter transfer function in frequency space [28,29] specific to each sensing sequence. Combining these with measurement results via a convex-optimization routine, we quantitatively reconstruct the noise spectrum. Our experiments using a single $^{171}Yb^{+}$ ion reveal previously unidentified narrowband spectral noise features on a radial mode that we probe with sensitivity to shifts in the mode frequency at the ∼0.5 Hz level [30].

A bichromatic light field with frequency components symmetrically detuned from the red and blue motional sideband transitions couples the ion's internal state to the oscillator mode via an interaction described by

$$\hat{H}(t) = \frac{1}{2}\hbar\eta\Omega(t)\hat{\sigma}_x\{e^{-i[\delta t+\phi(t)]}\hat{a}^\dagger + e^{i[\delta t+\phi(t)]}\hat{a}\}, \quad (1)$$

with Lamb-Dicke factor η, Rabi frequency $\Omega(t)$, and Pauli operator $\hat{\sigma}_x$ acting on the ion's internal state. The ion-oscillator coupling is captured by the creation and annihilation operators $\hat{a}^\dagger, \hat{a}$ and the time-dependent exponential that includes the angular frequency difference δ (detuning) of the bichromatic field from the mode resonance, as well as the phase difference $\phi(t) = [\phi_b(t) - \phi_r(t)]/2$ between the two frequency components (blue and red).

The fundamental principle of the noise-sensing protocol is illustrated in Fig. 1(a) using a phase space representation of an oscillator corotating reference frame. Initially, the

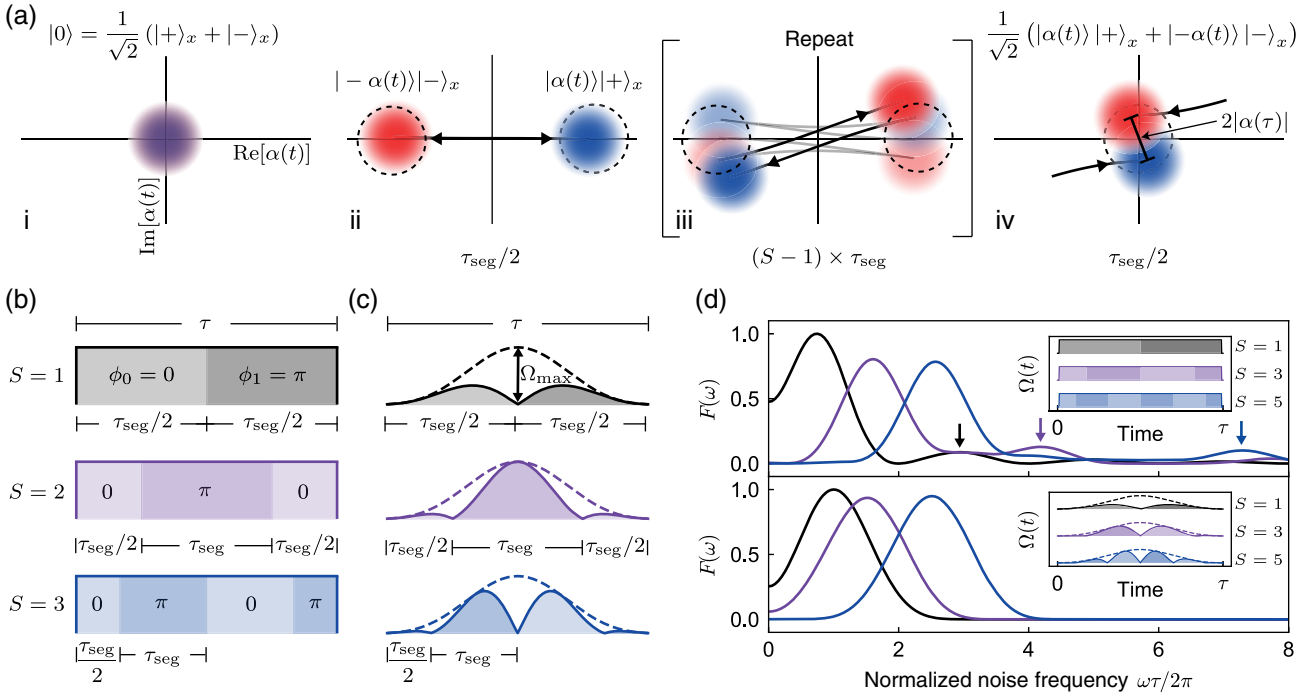

FIG. 1. (a) Schematic illustration of the noise sensing sequences in oscillator phase space. (a,i) A qubit is prepared in $|0\rangle$ and the oscillator in its ground state (wave packet centered at the origin). (a,ii) An initial displacement $\hat{D}[\hat{\alpha}(t)]$ of duration $\tau_{seg}/2$ splits the wave packet into two components associated with the $|+\rangle_x$ (blue) and $|-\rangle_x$ (red) internal qubit states, with the wave packets following trajectories indicated by the black lines. (a,iii) The wave packets are repeatedly displaced under π-phase inversion $(S-1)$ times for a duration of τ_{seg}. The nominally straight trajectory in each segment curves under the detuning noise, and the wave packets deviate from the nominal displacement at the conclusion of each segment (dashed circles). (a,iv) A final displacement of duration $\tau_{seg}/2$ recombines the wave packets up to an accumulated differential displacement $2|\alpha(\tau)|$. (b),(c) Schematic illustration of the fixed amplitude (square) and amplitude-modulated (Slepian) pulse profiles. The total sequence time τ and the number of phase shifts S determine the segment duration $\tau_{seg}=\tau/S$. The coupling phase in each segment alternates between 0 and π, indicated by light and dark shading, respectively. For the amplitude-modulated sequences, a Slepian envelope (dashed line) with an underlying cosinusoidal modulation is applied to the maximum Rabi frequency Ω_{max}. (d) Example filter functions $F(\omega)$ for the first three odd-S square sequences (top), with arrows indicating harmonics, and for the equivalent Slepian-modulated sequences (bottom), where the harmonics have been suppressed. The filter functions are plotted against the dimensionless quantity $\omega\tau/2\pi$, which is the noise frequency ω normalized to the sequence duration τ. Insets show the corresponding Rabi frequency $\Omega(t)$ and phase profiles.

ion's internal state encoding a qubit is prepared in $|0\rangle$ and the oscillator is brought close to its ground state [Fig. 1(a,i)]. The unitary evolution of the system under Eq. (1) enacts a qubit-state-dependent displacement of the motional wave packet [34,35] given by

$$\hat{D}[\hat{\alpha}(t)] = \exp\{\hat{\sigma}_x[\alpha(t)\hat{a}^\dagger - \alpha(t)^*\hat{a}]\}, \tag{2}$$

where the displacement $\alpha(t)$ at time τ is given by $\alpha(\tau) = -i\eta/2\int_0^\tau \Omega(t)e^{-i[\delta t+\phi(t)]}dt$. As the initial state $|0\rangle$ is a superposition in the displacement operator's x eigenbasis, the application of Eq. (2) splits the ion wave packet apart and creates an entangled state between the internal and oscillator degrees of freedom—a motional cat state, shown in Fig. 1(a,ii).

The sensing protocol is composed of an on-resonance ($\delta=0$), continuously driven state-dependent displacement with periodic discrete π shifts of the coupling phase $\phi(t)$, inverting the direction in phase space. This structure repeatedly displaces the split wave packets through the origin [Fig. 1(a,iii)]. Finally, the wave packets are brought back to the origin and, in the absence of noise, coherently reinterfere to restore the qubit state to $|0\rangle$. The presence of motional mode frequency fluctuations, however, will result in curved displacements, gradually decreasing the overlap and resulting in a separation of $2|\alpha(\tau)|$ at sequence end [Fig. 1(a,iv)]. This corresponds to residual qubit-oscillator entanglement and manifests as purity loss in projective measurements of the qubit. In the maximally mixed case of zero overlap between the wave packet components, the probability P_1 of finding the $|1\rangle$ state reaches 0.5.

Each sequence in Figs. 1(b) and 1(c) is defined by the total duration τ and the number of phase shifts S. The total sensing pulse of length τ consists of $S+1$ segments indexed by $s\in\{0,S\}$, each with duration τ_s and coupling phase ϕ_s according to

$$\tau_s = \begin{cases} \tau_{\mathrm{seg}}/2, & \text{if } s = 0, S \\ \tau_{\mathrm{seg}}, & \text{otherwise} \end{cases} \quad \text{and} \quad \phi_s = \begin{cases} 0, & \text{if } s = \text{even} \\ \pi, & \text{if } s = \text{odd} \end{cases},$$

where $\tau_{\mathrm{seg}} = \tau/S$ similar to a Carr-Purcell-Meiboom-Gill dynamical decoupling sequence [36]. The amplitude of the driving field may take the form of a flattop "square" shape with a constant Rabi frequency $\Omega(t) = \Omega_{\max}$ [Fig. 1(b)]. Alternatively, we may employ a smooth envelope determined by a modulated Slepian function [Fig. 1(c)], known to serve as a provably optimal bandlimited window in frequency space suppressing spectral leakage [25–27]. Here, the modulated Rabi frequency $\Omega(t) = \Omega_{\max}|v_m^{(0)}(N, W)\cos\{\omega_S t\}|$ consists of two components. The first is cosinusoidal with frequency $\omega_S = 2\pi(S/2\tau)$, matching the frequency of the alternating coupling phase. The second is an overall envelope defined by a zeroth-order Slepian $v_m^{(0)}(N, W)$, with sample number N and bandwidth W [30].

In a measurement after sequence application, the expected value of P_1 (the sensor signal) may be expressed [37] as the overlap integral of the noise power spectral density $S(\omega)$ and the sensing sequence's filter function $F(\omega)$ as

$$\mathbb{E}[P_1] = \frac{1}{2\pi}\int_{-\infty}^{\infty} d\omega S(\omega)F(\omega) \quad \text{with}$$
$$F(\omega) = \sum_k T_k \left| \frac{2\pi\eta_k}{2}\int_0^{\tau} dt\Omega(t)e^{-i[(\delta_k-\omega)t+\phi(t)]}t \right|^2. \quad (3)$$

The filter function, Eq. (3), describes the susceptibility of an operation to oscillator frequency noise at frequency ω summed over all oscillator modes k. Here, $T_k = 2(\bar{n}_k + 1/2)$ incorporates the average initial phonon occupancy $\bar{n}_k$ for each mode (typically $\bar{n}_k \sim 0.2$ in our experiments). The first-order filter function is valid under the assumption that the residual oscillator displacement is small and that the noise is "weak" (see [30]). In this Letter, we simplify the discussion by considering only a single mode, achieved by ensuring the oscillator mode frequencies are separated sufficiently such that driving a particular mode does not excite other modes. We focus exclusively on noise arising from fluctuations in the mode frequencies; it is assumed that amplitude noise on the drive field, to which the sequences are also susceptible, does not contain spectral components in the noise frequency domain of interest (see [30] for further discussion).

For a fixed sequence duration τ, increasing the number of phase shifts S in either sequence type shifts the sensitivity of the filter function to higher frequencies [Fig. 1(d)]. Peak sensitivity occurs near $\omega_{\mathrm{peak}} \approx 2\pi \times S/2\tau$, which applies to all Slepian-modulated cases with $S \geq 2$ and becomes increasingly accurate in the limit of large S for the square sequences. Increasing the sequence duration τ narrows the filter bandwidth $\Delta\omega$ (defined as the full width at half maximum), with $\Delta\omega \sim 1/\tau$. Because of the abrupt inversion of the drive direction at each phase shift, the frequency-space representation of square pulses exhibits higher order harmonics, which are suppressed under Slepian modulation.

We implement both approaches using a single $^{171}\mathrm{Yb}^+$ ion confined in a linear Paul trap (similar to [38]), with motional frequencies $\omega_{x,y,z} \approx \{1.6, 1.5, 0.5\}$ MHz. A qubit is encoded on the $|F = 0, m_F = 0\rangle \equiv |0\rangle$ and $|F = 1, m_F = 0\rangle \equiv |1\rangle$ hyperfine ground state levels, split by ~12.6 GHz. Doppler cooling, state preparation, and measurement are performed using a laser near 369.5 nm. Qubit and motional states are manipulated through stimulated Raman transitions [39] using two beams from a pulsed laser near 355 nm. We implement the state-dependent displacement by driving an acousto-optic modulator in one of the beams with a two-tone radio frequency signal, producing a bichromatic light field that simultaneously drives the red and blue sideband transitions on resonance.

We first demonstrate the ability to produce a tuneable frequency response to motional frequency noise. A system identification procedure consisting of single-tone modulation at frequency ω_{mod} with magnitude β_{mod} and phase ϕ_{mod} shifts the nominally resonant laser frequency components symmetrically around the motional sideband frequencies in the form of $\beta_{\mathrm{mod}}\sin(\omega_{\mathrm{mod}}t + \phi_{\mathrm{mod}})$. In a given sensing sequence, we average the measured P_1 over different phase values ϕ_{mod} to obtain the expected value $\mathbb{E}[P_1]$, which we compare to theoretical predictions. For square pulses of different S values, we see good agreement between experiment and theory [Fig. 2(a)]. In these experiments we are, in principle, able to measure single-frequency signals above measurement-infidelity limits corresponding to detunings of ~10 mHz, using sequences up to a duration of $\tau = 32$ ms and $\Omega_{\max}/2\pi = 30$ kHz [30].

Comparing the response of the two kinds of sensing sequences provides direct evidence of harmonic suppression in the filter function through Slepian amplitude-modulated waveforms. The data in Fig. 2(b) show that both sequences exhibit similar peak sensitivity at $\omega_{\mathrm{mod}}/2\pi \approx 1.8$ kHz, with additional sensitivity due to spectral leakage at $\omega_{\mathrm{mod}}/2\pi \approx 5.2$ kHz only present for the square sequence.

Moving on from these validations, we require a technique to convert from measurements of $\mathbb{E}[P_1]$ in the presence of an unknown noise environment to a quantitative estimate of the noise power spectrum. For a given set of filter functions F and a vector of phase-averaged $\mathbb{E}[P_1]$ values, denoted as $\boldsymbol{p}$, the noise power spectrum $\boldsymbol{s}$ may be inferred via the relation $\boldsymbol{p} = F\boldsymbol{s}$ [Fig. 3(a)]. We solve for $\boldsymbol{s}$ by employing an approach based on convex optimization [17] used for the first time in experiment here. In this framework, the noise spectrum $\boldsymbol{s}$ is estimated by minimizing the objective function

$$\min_{\boldsymbol{s}}(\|F\boldsymbol{s} - \boldsymbol{p}\|_2^2 + \lambda\|D\boldsymbol{s}\|_2^2), \boldsymbol{s} \geq \boldsymbol{0}. \quad (4)$$

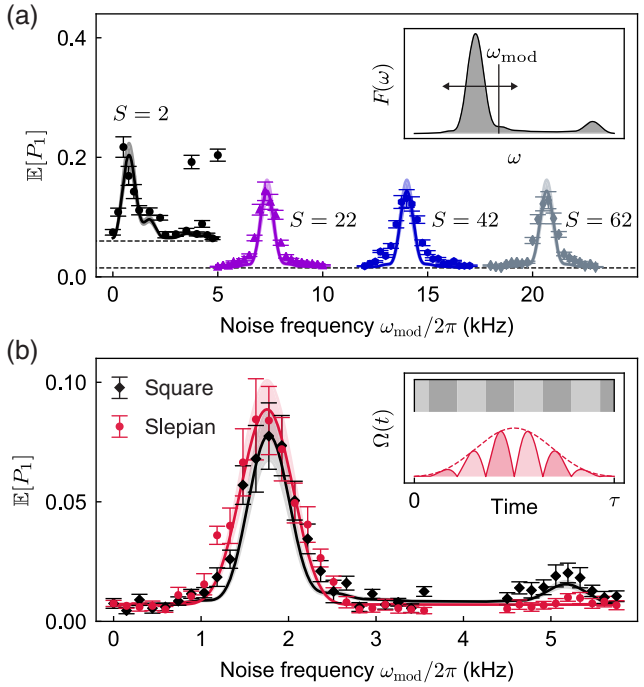

FIG. 2. System-identification experiments. (a) Response to engineered single-tone noise with a depth of $\beta_{\mathrm{mod}} = 40$ Hz for square sequences with $\tau = 1.5$ ms and $S = 2$, 22, 42, and 62. As illustrated in the inset, for each sequence the noise frequency ω_{mod} is scanned about the filter function peak. For the $S = 2$ data, this frequency range includes the first harmonic of $F(\omega)$ (small bump in inset); for the other sequences, this harmonic is not sampled. Experimental measurements of $\mathbb{E}[P_1]$ (markers) for each sequence are overlaid with filter function predictions (solid lines), including an additional frequency-independent offset (dashed horizontal lines). The additional offset for $S = 2$ is likely due to the dominant intrinsic noise contributions in the low frequency regime (cf. Fig. 3), with the two spurious points potentially due to a transient increase in intrinsic noise. (b) Comparison of the response to single-tone noise for a square (black, diamonds) and Slepian-modulated (red, circles) sequence with $\beta_{\mathrm{mod}} = 65$ Hz, $\tau = 2$ ms, and $S = 7$. The Rabi frequency for the Slepian sequence ($\Omega_{\mathrm{max}} = 2\pi \times 6.2$ kHz) is scaled relative to the square sequence ($\Omega_{\mathrm{max}} = 2\pi \times 2.6$ kHz) in order to match peak sensitivity between the protocols. In both panels, error bars are the standard error of the mean of the phase samples averaged to give $\mathbb{E}[P_1]$, and the shaded regions show uncertainty in the filter function prediction for a variation of $\bar{n} \pm 0.1$. The inset compares the Rabi frequency profile of the two sequences, with light and dark shading illustrating the alternating coupling phase.

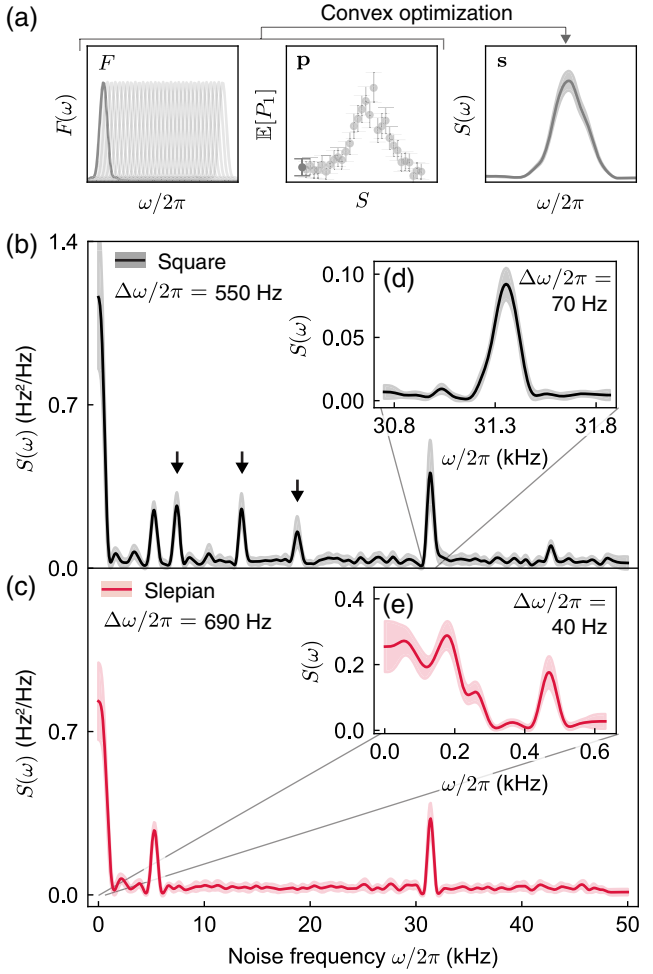

FIG. 3. (a) Schematic of the noise reconstruction algorithm. A set of sequences described by filter functions F produces a set of measurements $\boldsymbol{p}$. The noise spectrum $\mathbf{s}$ and associated uncertainty (shading) is determined by minimizing objective function Eq. (4). (b),(c) Reconstructed intrinsic noise power spectral density $S(\omega)$, comparing square (b) and Slepian (c) sequences with $1 \leq S \leq 193$ and $\tau = 2$ ms with spectral resolution $\Delta\omega/2\pi$. The maximum Rabi frequencies used were $\Omega_{\mathrm{max}} = 2\pi \times 9$ kHz for (b) and $\Omega_{\mathrm{max}} = 2\pi \times 20$ kHz for (c). Features present only in the square reconstruction are indicated by black arrows. The insets (d),(e) show reconstructions performed using higher spectral resolution sequences. The feature at ~31.4 kHz is probed with $\tau = 16$ ms, $986 \leq S \leq 1018$, and $\Omega_{\mathrm{max}} = 2\pi \times 0.9$ kHz (d). The low frequency regime (e) is probed using Slepian sequences with $\tau = 32$ ms, $1 \leq S \leq 37$, and a reduced $\Omega_{\mathrm{max}} = 2\pi \times 0.3$ kHz. Reducing Ω_{max} ensures that the sensor response remains in the small-signal regime prior to the onset of distortion due to higher-order filter terms, given by $\mathbb{E}[P_1] \lesssim 0.1$ [40,41].

The term $\lambda \|D\boldsymbol{s}\|_2^2$ is a regularization term where D is the first-order derivative operator (minimizing $\|D\boldsymbol{s}\|_2^2$ enforces smoothness in $\boldsymbol{s}$) and λ is a hyperparameter tuned via a standard method to prevent under or overfitting [30]; a strict-positivity requirement prevents overfitting-induced oscillations [17]. This convex-optimization approach to spectrum estimation enables the use of arbitrary sets of measurements with no requirements on the underlying measurement probe structures unlike in dynamical decoupling-based spectroscopy [42,43].

We use these techniques to detect and spectrally reconstruct intrinsic frequency noise on the ion's radial motion. In Figs. 3(b) and 3(c), we sample noise in the band from zero to 50 kHz, comparing the reconstructions returned

using both square and Slepian-modulated sequences. We see a strong low-frequency signal that dominates the measured system performance, as well as a number of well defined noise features common to both datasets. The insets [Figs. 3(d) and 3(e)] show higher-spectral-resolution reconstructions of specific noise features achieved by a combination of frequency shifting and increasing the pulse duration to narrow the filter bandwidth. The ability to arbitrarily shift the filter band and resolution—subject to hardware constraints—enables the noise spectrum to be probed in an iterative manner after identification of coarse spectral features [26,27].

The peak height $S(\omega_{\mathrm{peak}})$ of the *discrete* features present in the reconstructed spectra may be related to a motional frequency deviation $\pm\beta_{\mathrm{dev}}$ Hz by taking into account the effect of the filter bandwidth $\Delta\omega$ using $\beta_{\mathrm{dev}} \approx \sqrt{2S(\omega_{\mathrm{peak}})(\Delta\omega/2\pi)}$, giving $\beta_{\mathrm{dev}} \sim 10$–$20$ Hz for the observed features in Figs. 3(b) and 3(c). The sensitivity of the sequences employed in Figs. 3(b) and 3(c) is such that, in principle, the smallest detectable motional frequency deviations correspond to ~ 7 Hz for discrete and ~ 0.3 Hz for spectrally broad features. We have determined that the peaks near 5 kHz and 31 kHz likely arise from electromagnetic pickup in either the resonator stabilization circuit or the trap itself, having independently observed transient electromagnetic signals in the laboratory close to these frequencies. Further, frequency-resolved analysis of laser light shows no amplitude fluctuations commensurate with these features. We associate the additional spectral peaks present only in Fig. 3(b) with the sampling of out-of-band noise by the higher harmonics in the square sequences' filter functions, or amplitude noise caused by rapid phase transients in acousto-optic modulators that are suppressed by Slepian pulse modulation. See [30] for further discussion on laser-amplitude noise, measurement sensitivity, and the effects of sensor bandwidth.

In this Letter, we have demonstrated that sequences of periodically inverted qubit-state-dependent oscillator wave packet displacements provide a flexible means for performing noise spectroscopy on quantum oscillator modes via the creation of tuneable, bandlimited filters for mode-frequency noise. The technique is readily implementable in trapped-ion systems as it leverages the same interaction used to perform the ubiquitous Mølmer-Sørensen gate, enabling *in situ* noise characterization with no additional hardware resources. We have employed this technique to sense noise on the radial motion of a single trapped ion in a spectral range from quasi-dc to 50 kHz, combining two distinct sensing waveforms with a convex-optimization approach to spectrum estimation. In conjunction with previously reported modulation and robustness protocols [37,44–57], our sensing technique provides a tool for designing gate operations in trapped-ion systems with robustness tailored to a specific noise environment.

This work was partially supported by the Intelligence Advanced Research Projects Activity Grant No. W911NF-16-1-0070, the US Army Research Office Grant No. W911NF-14-1-0682, the Australian Research Council Centre of Excellence for Engineered Quantum Systems Grant No. CE170100009, and a private grant from H.&A. Harley.

A. R. M. and C. H. contributed equally to this work.

*Corresponding author.
alistair.r.milne@gmail.com
†Corresponding author.
michael.biercuk@sydney.edu.au
‡Present address: Paul Scherrer Institute, 5232 Villigen PSI, Switzerland.

[1] J. I. Cirac and P. Zoller, Phys. Rev. Lett. **74**, 4091 (1995).
[2] C. A. Sackett, D. Kielpinski, B. E. King, C. Langer, V. Meyer, C. J. Myatt, M. Rowe, Q. A. Turchette, W. M. Itano, D. J. Wineland, and C. Monroe, Nature (London) **404**, 256 (2000).
[3] D. Leibfried, B. DeMarco, V. Meyer, D. Lucas, M. Barrett, J. Britton, W. M. Itano, B. Jelenković, C. Langer, T. Rosenband, and D. J. Wineland, Nature (London) **422**, 412 (2003).
[4] F. Schmidt-Kaler, H. Hffner, M. Riebe, S. Gulde, G. P. T. Lancaster, T. Deuschle, C. Becher, C. F. Roos, J. Eschner, and R. Blatt, Nature (London) **422**, 408 (2003).
[5] A. W. Cross and J. M. Gambetta, Phys. Rev. A **91**, 032325 (2015).
[6] H. Paik, A. Mezzacapo, M. Sandberg, D. T. McClure, B. Abdo, A. D. Corcoles, O. Dial, D. F. Bogorin, B. L. T. Plourde, M. Steffen, A. W. Cross, J. M. Gambetta, and J. M. Chow, Phys. Rev. Lett. **117**, 250502 (2016).
[7] C. Song, S.-B. Zheng, P. Zhang, K. Xu, L. Zhang, Q. Guo, W. Liu, D. Xu, H. Deng, K. Huang, D. Zheng, X. Zhu, and H. Wang, Nat. Commun. **8**, 1061 (2017).
[8] A. Blais, S. M. Girvin, and W. D. Oliver, Nat. Phys. **16**, 247 (2020).
[9] F. Borjans, X. G. Croot, X. Mi, M. J. Gullans, and J. R. Petta, Nature (London) **577**, 195 (2020).
[10] M. Aspelmeyer, T. J. Kippenberg, and F. Marquardt, Rev. Mod. Phys. **86**, 1391 (2014).
[11] C. Flühmann, T. L. Nguyen, M. Marinelli, V. Negnevitsky, K. Mehta, and J. P. Home, Nature (London) **566**, 513 (2019).
[12] P. Campagne-Ibarcq, A. Eickbusch, S. Touzard, E. Zalys-Geller, N. E. Frattini, V. V. Sivak, P. Reinhold, S. Puri, S. Shankar, R. J. Schoelkopf, L. Frunzio, M. Mirrahimi, and M. H. Devoret, Nature (London) **584**, 368 (2020).
[13] D. Gottesman, A. Kitaev, and J. Preskill, Phys. Rev. A **64**, 012310 (2001).
[14] K. C. McCormick, J. Keller, D. J. Wineland, A. C. Wilson, and D. Leibfried, Quantum Sci. Technol. **4**, 024010 (2019).
[15] J. Keller, P.-Y. Hou, K. C. McCormick, D. C. Cole, S. D. Erickson, J. J. Wu, A. C. Wilson, and D. Leibfried, following Letter, Phys. Rev. Lett. **126**, 250507 (2021).

[16] K. C. McCormick, J. Keller, S. C. Burd, D. J. Wineland, A. C. Wilson, and D. Leibfried, Nature (London) **572**, 86 (2019).

[17] H. Ball, M. Biercuk, A. Carvalho, J. Chen, M. R. Hush, L. A. de Castro, L. Li, P. J. Liebermann, H. Slatyer, C. Edmunds, V. Frey, C. Hempel, and A. Milne, Quantum Sci. Technol. (2021), https://doi.org/10.1088/2058-9565/abdca6.

[18] D. J. Wineland, Rev. Mod. Phys. **85**, 1103 (2013).

[19] C. Monroe, D. M. Meekhof, B. E. King, and D. J. Wineland, Science **272**, 1131 (1996).

[20] H.-Y. Lo, D. Kienzler, L. de Clercq, M. Marinelli, V. Negnevitsky, B. C. Keitch, and J. P. Home, Nature (London) **521**, 336 (2015).

[21] B. Vlastakis, G. Kirchmair, Z. Leghtas, S. E. Nigg, L. Frunzio, S. M. Girvin, M. Mirrahimi, M. H. Devoret, and R. J. Schoelkopf, Science **342**, 607 (2013).

[22] B. Hacker, S. Welte, S. Daiss, A. Shaukat, S. Ritter, L. Li, and G. Rempe, Nat. Photonics **13**, 110 (2019).

[23] W. S. Leong, M. Xin, Z. Chen, S. Chai, Y. Wang, and S.-Y. Lan, Nat. Commun. **11**, 5295 (2020).

[24] C. Hempel, B. P. Lanyon, P. Jurcevic, R. Gerritsma, R. Blatt, and C. F. Roos, Nat. Photonics **7**, 630 (2013).

[25] V. M. Frey, S. Mavadia, L. M. Norris, W. d. Ferranti, D. Lucarelli, L. Viola, and M. J. Biercuk, Nat. Commun. **8**, 2189 (2017).

[26] L. M. Norris, D. Lucarelli, V. M. Frey, S. Mavadia, M. J. Biercuk, and L. Viola, Phys. Rev. A **98**, 032315 (2018).

[27] V. Frey, L. M. Norris, L. Viola, and M. J. Biercuk, Phys. Rev. Applied **14**, 024021 (2020).

[28] T. J. Green, J. Sastrawan, H. Uys, and M. J. Biercuk, New J. Phys. **15**, 095004 (2013).

[29] G. A. Paz-Silva and L. Viola, Phys. Rev. Lett. **113**, 250501 (2014).

[30] See Supplemental Material, which includes Refs. [31–33], at http://link.aps.org/supplemental/10.1103/PhysRevLett.126.250506 for information on filter function prediction error scaling; sequence sensitivity limits; the effects of finite filter bandwidth; estimating ion temperature; a detailed description of the Slepian sequences and of the spectrum reconstruction algorithm; and for further details relating to the intrinsic noise reconstruction, including a discussion of the effects of laser amplitude noise.

[31] A. Tarantola, *Inverse Problem Theory And Methods For Model Parameter Estimation*, Vol. 89 (SIAM, Philadelphia, 2005).

[32] A. N. Tikhonov, Sov. Math. Dokl. **4**, 1035 (1963).

[33] T. Hastie, R. Tibshirani, and J. Friedman, *The Elements of Statistical Learning* (Springer, New York, USA, 2009).

[34] C. F. Roos, New J. Phys. **10**, 013002 (2008).

[35] G. Kirchmair, J. Benhelm, F. Zähringer, R. Gerritsma, C. F. Roos, and R. Blatt, New J. Phys. **11**, 023002 (2009).

[36] S. Meiboom and D. Gill, Rev. Sci. Instrum. **29**, 688 (1958).

[37] A. R. Milne, C. L. Edmunds, C. Hempel, F. Roy, S. Mavadia, and M. J. Biercuk, Phys. Rev. Applied **13**, 024022 (2020).

[38] M. Guggemos, Ph.D. thesis, University of Innsbruck, 2017.

[39] D. Hayes, D. N. Matsukevich, P. Maunz, D. Hucul, Q. Quraishi, S. Olmschenk, W. Campbell, J. Mizrahi, C. Senko, and C. Monroe, Phys. Rev. Lett. **104**, 140501 (2010).

[40] T. Green, H. Uys, and M. J. Biercuk, Phys. Rev. Lett. **109**, 020501 (2012).

[41] A. Soare, H. Ball, D. Hayes, J. Sastrawan, M. C. Jarratt, J. J. McLoughlin, X. Zhen, T. J. Green, and M. J. Biercuk, Nat. Phys. **10**, 825 (2014).

[42] G. A. Alvarez and D. Suter, Phys. Rev. Lett. **107**, 230501 (2011).

[43] J. Bylander, S. Gustavsson, F. Yan, F. Yoshihara, K. Harrabi, G. Fitch, D. G. Cory, Y. Nakamura, J.-S. Tsai, and W. D. Oliver, Nat. Phys. **7**, 565 (2011).

[44] D. Hayes, S. M. Clark, S. Debnath, D. Hucul, I. V. Inlek, K. W. Lee, Q. Quraishi, and C. Monroe, Phys. Rev. Lett. **109**, 020503 (2012).

[45] T. Choi, S. Debnath, T. A. Manning, C. Figgatt, Z. X. Gong, L. M. Duan, and C. R. Monroe, Phys. Rev. Lett. **112**, 190502 (2014).

[46] F. Haddadfarshi and F. Mintert, New J. Phys. **18**, 123007 (2016).

[47] T. Manovitz, A. Rotem, R. Shaniv, I. Cohen, Y. Shapira, N. Akerman, A. Retzker, and R. Ozeri, Phys. Rev. Lett. **119**, 220505 (2017).

[48] Y. Shapira, R. Shaniv, T. Manovitz, N. Akerman, and R. Ozeri, Phys. Rev. Lett. **121**, 180502 (2018).

[49] P. H. Leung, K. A. Landsman, C. Figgatt, N. M. Linke, C. R. Monroe, and K. R. Brown, Phys. Rev. Lett. **120**, 020501 (2018).

[50] P. H. Leung and K. R. Brown, Phys. Rev. A **98**, 032318 (2018).

[51] A. E. Webb, S. C. Webster, S. Collingbourne, D. Bretaud, A. M. Lawrence, S. Weidt, F. Mintert, and W. K. Hensinger, Phys. Rev. Lett. **121**, 180501 (2018).

[52] G. Zarantonello, H. Hahn, J. Morgner, M. Schulte, A. Bautista-Salvador, R. F. Werner, K. Hammerer, and C. Ospelkaus, Phys. Rev. Lett. **123**, 260503 (2019).

[53] L. Yao, S. Zhang, K. Zhang, W. Chen, Y. Shen, J. Zhang, J. Zhang, and K. Kim, Nature (London) **572**, 363 (2019).

[54] T. J. Green and M. J. Biercuk, Phys. Rev. Lett. **114**, 120502 (2015).

[55] K. A. Landsman, Y. Wu, P. H. Leung, D. Zhu, N. M. Linke, K. R. Brown, L. Duan, and C. Monroe, Phys. Rev. A **100**, 022332 (2019).

[56] Y. Shapira, R. Shaniv, T. Manovitz, N. Akerman, L. Peleg, L. Gazit, R. Ozeri, and A. Stern, Phys. Rev. A **101**, 032330 (2020).

[57] N. Grzesiak, R. Blümel, K. Wright, K. M. Beck, N. C. Pisenti, M. Li, V. Chaplin, J. M. Amini, S. Debnath, J.-S. Chen, and Y. Nam, Nat. Commun. **11**, 2963 (2020).